universe

MDPI

Article

Reconstruction and Identification of High-Q^2 Elastic ep Events at EicC

Wan Chang [1], Yutie Liang [2] and Weizhi Xiong [3,*]

[1] School of Physics and Electronic Engineering, Nanyang Normal University, Nanyang 473061, China; changwan@nynu.edu.cn
[2] Institute of Modern Physics, Chinese Academy of Sciences, Lanzhou 730000, China; liangyt@impcas.ac.cn
[3] Key Laboratory of Particle Physics and Particle Irradiation (MOE), Institute of Frontier and Interdisciplinary Science, Shandong University, Qingdao 266237, China
* Correspondence: xiongw@sdu.edu.cn

Abstract

Understanding the internal structure of a proton remains a central objective of modern nuclear physics. Measurements of unpolarized elastic electron–proton scattering at high four-momentum transfer, Q^2, provide essential input for determining proton electromagnetic form factors. The proposed Electron–Ion Collider in China (EicC), with its broad kinematic coverage and advanced detector capabilities, offers a promising opportunity to study elastic scattering in this kinematic region. In this work, we present a feasibility study of high-Q^2 unpolarized elastic electron–proton scattering at EicC. Particular attention is given to the reconstruction of elastic events and the suppression of inelastic backgrounds using kinematic constraints, with the aim of assessing whether a clean elastic event sample can be obtained.

Keywords: EicC; ep elastic scattering; electromagnetic form factor

1. Introduction

Understanding the internal structure of a proton remains a central topic in modern hadronic physics. Elastic electron–proton (ep) scattering offers a clean and well-controlled tool for investigating a proton's electromagnetic structure, which is characterized by electric and magnetic form factors, G_E and G_M [1–6]. These form factors encode information on the spatial distributions of electric charge and magnetization of a proton [7–17], thereby providing insight into the underlying quark–gluon dynamics governed by QCD. At high four-momentum transfer, Q^2, proton electromagnetic form factors provide a stringent testing ground for QCD-based descriptions of nucleon structure. Their behavior is sensitive to short-distance quark dynamics, the possible onset of perturbative-QCD scaling, quark orbital angular momentum, and the transition between nonperturbative and perturbative regimes. A variety of theoretical frameworks have made predictions for the high-Q^2 behaviors of these form factors, including perturbative-QCD-based approaches [18,19], continuum QCD calculations based on Dyson–Schwinger equations [20–22], light front holographic QCD [23], and lattice QCD calculations [24–26]. Precision measurements in this kinematic region are therefore essential for discriminating among different theoretical descriptions and for clarifying how the observed nucleon form factors emerge from the underlying quark and gluon degrees of freedom.

Check for updates

Academic Editor: Máté Csanád

Received: 12 August 2026
Revised: 14 September 2026
Accepted: 15 September 2026
Published: 17 September 2026

Copyright: © 2026 by the authors. Licensee MDPI, Basel, Switzerland. This article is an open access article distributed under the terms and conditions of the Creative Commons Attribution (CC BY) license.

Over the past several decades, measurements of unpolarized elastic cross sections and polarization observables have substantially improved our knowledge of G_E and G_M. Nevertheless, there are still important inconsistencies. Most notably, the ratio $\mu_p G_E/G_M$, where μ_p is the proton magnetic moment, differs when extracted using Rosenbluth separation- and polarization-based methods, particularly at moderate and high Q^2 levels [27–33]. Although two photon exchange corrections can account for part of this discrepancy, further measurements with improved precision and extended kinematic coverage remain necessary [34–39].

Ongoing research at Jefferson Lab [40,41] and proposed measurements at the U.S. Electron–Ion Collider (EIC) [42,43] aim to extend elastic scattering studies to higher Q^2 using high-energy beams and advanced detector systems. At large Q^2, however, the rapidly decreasing elastic cross section makes such measurements increasingly challenging. Their precision can also be limited by systematic uncertainties associated with luminosity determination, detector acceptance and resolution, radiative corrections, and background subtraction. Measurements using complementary beam energies and detector configurations are therefore valuable for developing a comprehensive and internally consistent understanding of the proton electromagnetic form factors.

The proposed Electron–Ion Collider in China (EicC) [44] is designed to enable high-precision studies of hadron structures. It is expected to operate at center-of-mass energies of approximately 15–20 GeV, with a design luminosity above 10^{33} cm^{-2} s^{-1}. The EicC will therefore occupy a kinematic regime between the fixed-target program at Jefferson Lab and the higher-energy U.S. EIC, providing complementary access to moderate- and high-Q^2 nucleon structures. Its combination of high luminosity and collider kinematics offers an opportunity to extend elastic ep measurements beyond the traditional fixed-target domain. In addition, the conceptual EicC central detector provides broad pseudo-rapidity coverage, approximately $-3.5 < \eta < 3.5$, together with high-resolution charged-particle tracking. These capabilities may allow both a scattered electron and a recoil proton to be reconstructed with high precision, and the overconstrained elastic kinematics to be used to suppress inelastic backgrounds.

In this paper, we investigate the feasibility of measuring unpolarized elastic ep scattering at the EicC, with particular emphasis on determining whether a clean elastic event sample can be isolated from inelastic backgrounds. Section 2 presents the expected event yields and kinematic distributions for the considered EicC beam configuration, including the accessible Q^2 range and production rates for an integrated luminosity of 100 fb^{-1}. Section 3 introduces the conceptual EicC detector design and the detector subsystems relevant to this study. Section 4 examines the reconstruction of elastic kinematics using both a scattered electron and a recoil proton. Section 5 evaluates the separation of elastic events from inelastic backgrounds through a set of kinematic and event topology selection criteria. Finally, Section 6 summarizes the main findings and discusses their implications for possible future measurements of the proton electromagnetic form factors at EicC.

The results of this study provide an initial assessment of the experimental feasibility of identifying high-Q^2 elastic ep events at the EicC. They also illustrate the importance of reconstructing both final-state particles and provide guidance for detector and analysis requirements relevant to a future elastic scattering program.

2. Kinematics and Elastic Cross Section

To evaluate the prospects of measuring elastic ep scattering at the EicC, we first calculate the expected elastic event yields and the corresponding final-state kinematics. Unless otherwise stated, the calculations are performed for the nominal EicC beam energy configuration, with a 3.5 GeV electron beam colliding with a 20 GeV proton beam. The inte-

grated luminosity is taken to be 100 fb^{-1}. The tree-level differential cross section of elastic ep scattering can be expressed in a Lorentz-invariant form as [43]

$$\frac{d\sigma}{dQ^2} = \frac{4\pi\alpha^2}{Q^4}\left[\frac{G_E^2 + \tau G_M^2}{1+\tau}\left(1 - y - \frac{M_p^2 y^2}{Q^2}\right) + \frac{1}{2}y^2 G_M^2\right]. \quad (1)$$

Here Q^2 is the negative of the momentum transfer squared between the incoming and outgoing electron, α is the electromagnetic fine-structure constant, y is the inelasticity and is identified as the fraction of the electron energy taken by the exchanged photon in the proton rest frame, M_p is the proton mass, and $\tau \equiv Q^2/(4M_p^2)$.

Figure 1 shows the expected number of elastic events as a function of Q^2, using the Kelly form factor parameterization [45]. The yield decreases rapidly with increasing Q^2, as expected from the elastic cross section. Nevertheless, the statistics remain sizable over a broad kinematic range. For example, the expected yield around $Q^2 = 5$ GeV^2 is of order 10^6 events per 1 GeV^2 bin for 100 fb^{-1}. Although the event rate becomes increasingly limited with higher momentum transfers, the projected yields suggest that the elastic channel could be investigated up to approximately $Q^2 = 40$ GeV^2 with suitable binning.

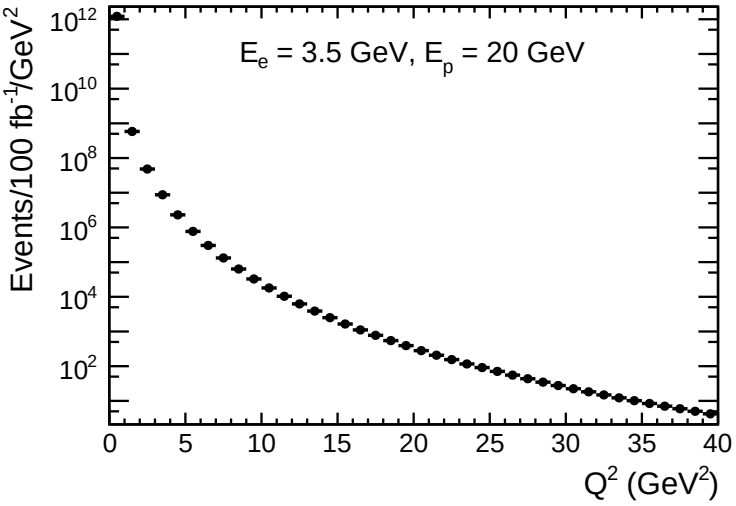


Figure 1. Expected number of elastic ep events as a function of Q^2 for an integrated luminosity of 100 fb^{-1} and a Q^2 bin width of 1 GeV^2.

The kinematic properties of the outgoing particles determine the detector acceptance required for the measurement. At the EicC, the incoming proton is defined to travel along the positive z direction, and all kinematic variables are measured within this coordinate system. Figure 2 shows the pseudo-rapidity of scattered electrons and recoil protons as functions of Q^2. As Q^2 increases, the scattered electron moves from the electron-going backward region toward central pseudo-rapidity. Its pseudo-rapidity increases from approximately -1.5 at $Q^2 = 2$ GeV^2 to approximately 0 at $Q^2 = 40$ GeV^2. In contrast, the recoil proton remains in the forward, ion-going region, with its pseudo-rapidity decreasing from approximately 3.2 to 1.8 over the same Q^2 range. The energies of the outgoing electron and proton as functions of Q^2 are presented in Figure 3. The scattered electron energy increases with Q^2, from approximately 3.6 GeV at $Q^2 = 2$ GeV^2 to approximately 5.8 GeV at $Q^2 = 40$ GeV^2. The recoil proton energy decreases correspondingly from approximately 20 GeV to 18 GeV over the same range.

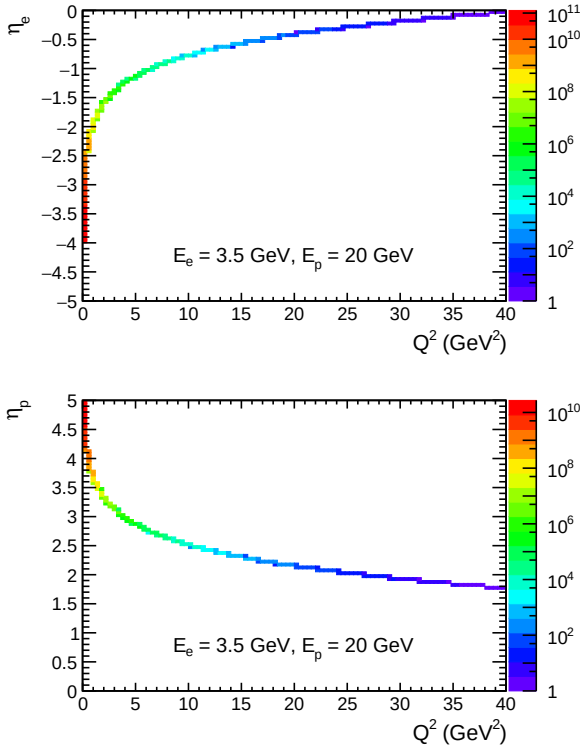


Figure 2. The correlation between pseudo-rapidity and Q^2 shown for scattered electrons (**top**) and recoil protons (**bottom**).

The kinematic correlations in Figures 2 and 3, together with the production rates in Figure 1, define the basic experimental requirements for studying elastic ep scattering at the EicC. In principle, because elastic scattering is a two-body process, the event kinematics can be reconstructed from either the scattered electron or the recoil proton alone, provided that the event has already been identified as elastic. In practice, however, the main experimental challenges are to distinguish elastic events from inelastic backgrounds and to reconstruct the elastic signal with sufficient resolution. These challenges are particularly relevant in collider kinematics, where elastic events occur at small y and single-arm reconstruction methods can be highly sensitive to detector resolution [43]. When both scattered electrons and recoil protons are detected, their measured angles can be used in the double-angle (DA) method to reconstruct the event kinematics (details discussed in Section 4). Because this method relies primarily on angular measurements, it can provide better resolutions in Q^2 and x than single-arm reconstruction methods. In addition, reconstructing both final-state particles overconstrains the elastic two-body topology. Angular correlations, transverse-momentum balance, energy and longitudinal-momentum conservation, and reconstructed elastic observables can therefore be combined to distinguish elastic events from inelastic backgrounds and improve the robustness of the event selection.

Beyond determining the requirements for event reconstruction and background suppression, the accessible kinematics also determine the relative sensitivity of the unpolarized elastic cross section to the proton electric and magnetic form factors. It is therefore useful to examine the virtual-photon polarization parameter ε, which governs the relative contributions of G_E and G_M and determines whether a Rosenbluth separation can be performed. In the one-photon-exchange approximation, the reduced elastic cross section is conventionally written as

$$\sigma_R = \tau G_M^2(Q^2) + \varepsilon G_E^2(Q^2). \quad (2)$$

Measurements at the same Q^2 but over a sufficiently broad range of ε allow the electric and magnetic contributions to be separated. Specifically, a linear fit of σ_R as a function of ε has an intercept of τG_M^2 and a slope of G_E^2. Although the reduced cross section formalism is commonly introduced in the proton rest frame using fixed-target kinematics, an analogous reduced cross section can be defined for collider kinematics, and the quantities Q^2, τ, and ε can be expressed in terms of Lorentz invariants. The separation of the electric and magnetic contributions is therefore not restricted to fixed-target experiments. For collider kinematics, the virtual-photon polarization parameter can be written as [43]

$$\varepsilon = \frac{1 - y - \frac{1}{4}\gamma^2 y^2}{1 - y + \frac{1}{4}y^2(\gamma^2 + 2)}, \tag{3}$$

where $\gamma^2 = Q^2/\nu^2$ and ν is the energy transfer in the proton rest frame. For elastic scattering, $\nu = Q^2/(2M_p)$. Because elastic events at the EicC occur at relatively small y, the corresponding values of ε remain close to unity. This behavior is illustrated in Figure 4, which compares the nominal configuration of 3.5 GeV electrons colliding with 20 GeV protons with a possible lower center-of-mass energy configuration of 2.8 GeV electrons colliding with 12 GeV protons. Although the lower-energy configuration shifts ε slightly away from unity, the accessible events still occupy only a narrow high-ε region. As also found in studies of elastic scattering at the U.S. EIC [43], the EicC could provide valuable elastic cross section data at high ε. Although the limited ε coverage prevents an independent Rosenbluth separation of G_E and G_M for the beam energy configurations considered here, these measurements would constrain the combination $\tau G_M^2 + \varepsilon G_E^2$, and contribute to global form-factor analyses when combined with existing cross section and polarization data [34,39]. The present study therefore focuses on the reconstruction and isolation of elastic events rather than on extracting proton electromagnetic form factors through a Rosenbluth separation.

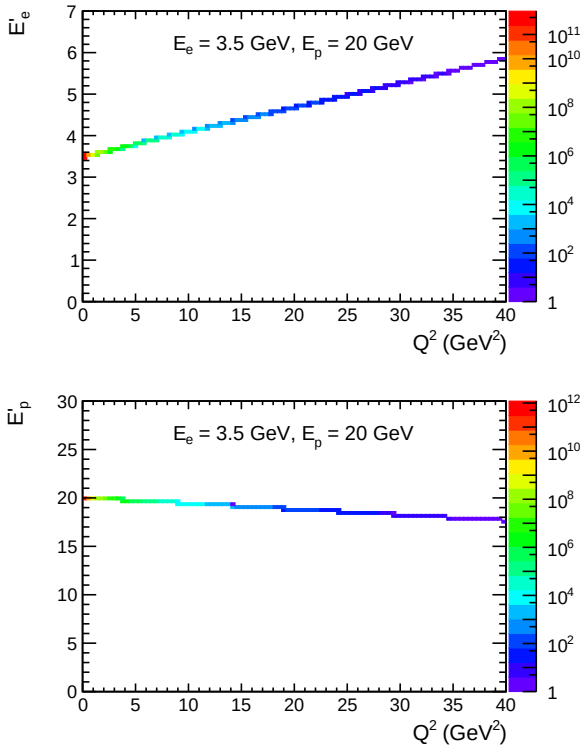


Figure 3. The correlation between energy and Q^2 shown for scattered electrons (**top**) and recoil protons (**bottom**).

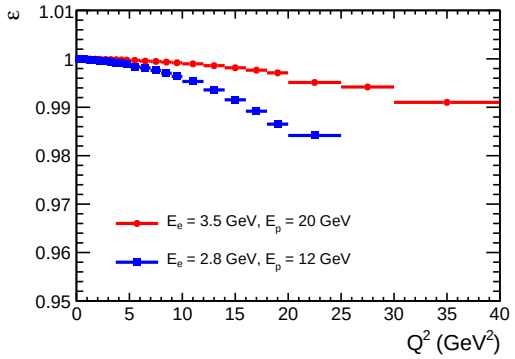


Figure 4. The distributions of ε as a function of Q^2 of elastic ep events with 3.5 GeV on 20 GeV (red curve) and 2.8 GeV on 12 GeV (blue curve).

3. Detector

The EicC detector is designed to provide broad angular coverage for the reconstruction and identification of final-state particles produced in electron–proton and electron–ion collisions. For the elastic ep process considered in this work, the principal detector requirements are precise charged-particle tracking, reliable electron identification, and sufficient angular acceptance to reconstruct scattered electrons and recoil protons in coincidence. The conceptual detector layout is shown in Figure 5. It consists of a central detector surrounding the interaction point, complemented by several ion far-forward detector subsystems located along the outgoing proton beam direction.

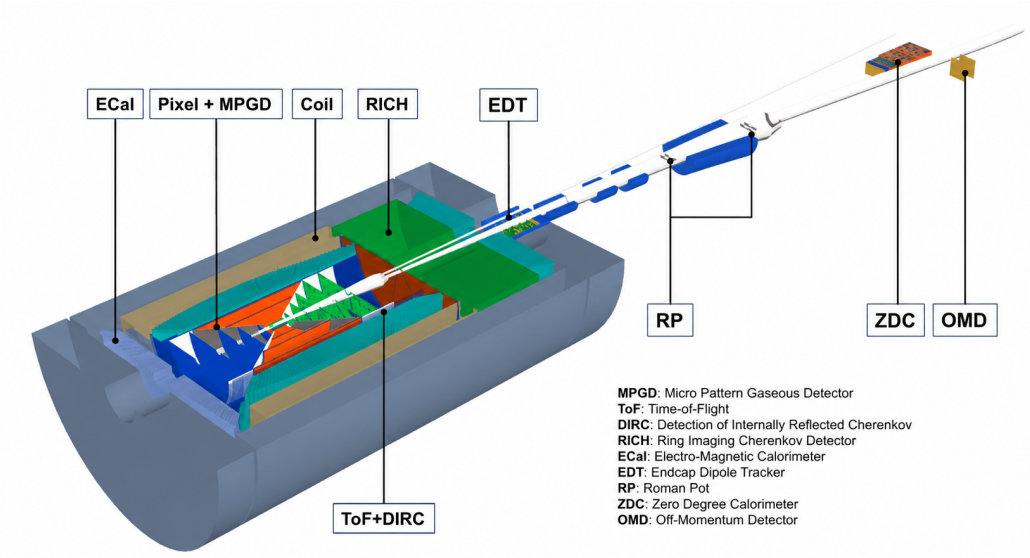


Figure 5. Conceptual layout of the EicC detector, including the central detector and ion far-forward detector systems.

The central detector provides full azimuthal acceptance over a pseudo-rapidity range of approximately $-3.5 < \eta < 3.5$. Charged-particle tracking is provided by a silicon-pixel vertex detector together with several Micro-Pattern Gaseous Detector (MPGD) tracking layers. These tracking systems are located within the solenoidal magnetic field of the central magnet, enabling the reconstruction of charged-particle trajectories and momenta. For the kinematic region emphasized in this study, particularly $Q^2 > 2$ GeV^2, the scattered electron is emitted into the backward-to-central region, whereas the recoil proton is detected predominantly in the ion-endcap region of the central detector. The broad angular coverage

therefore allows both final-state particles to be reconstructed over most of the kinematic range considered.

Particle identification (PID) is provided by several complementary detector subsystems. The electromagnetic calorimeter [46] measures the scattered electron energy and provides the principal information for electron identification, while Ring-Imaging Cherenkov (RICH) detectors provide hadron identification capability, particularly in the forward region. In the ion endcap, however, the baseline PID system is expected to distinguish hadrons only up to momenta of approximately 15 GeV/c [47]. For the elastic ep kinematics studied here, the recoil proton typically has a momentum above this range. The present analysis therefore does not rely primarily on direct proton identification by the dedicated PID detectors. Instead, the recoil proton candidate is identified using charged-particle tracking together with the strong kinematic constraints of the elastic two-body final state. In particular, the coincidence of an electron candidate with a forward charged track, combined with angular correlations, transverse momentum balance, momentum consistency, and reconstructed elastic observables, provides the main basis for selecting elastic events and suppressing inelastic backgrounds.

The EicC design also includes several ion far-forward detector systems, including the Endcap Dipole Tracker (EDT), Roman Pots (RPs), Off-Momentum Detector (OMD), and Zero Degree Calorimeter (ZDC). These detectors are important for the broader EicC forward physics program but are not the primary focus of the present study, which mainly considers events in which both scattered electrons and recoil protons are reconstructed within the central-detector acceptance. The EDT and RP could, in principle, extend the acceptance for recoil protons emitted at very small angles, particularly at lower Q^2. Such events are accompanied by electrons scattered into the far-backward region, however, and the corresponding detector acceptance and reconstruction performance have not been evaluated in detail in this work. The OMD and ZDC are not expected to contribute directly to the reconstruction of the elastic events considered here.

In the present study, the detector response is modeled using a fast simulation based on the expected performance of the EicC detector. Tracking efficiencies and resolutions are taken from detector studies employing the GENFIT reconstruction package [48]. Charged particles within the central-detector acceptance are reconstructed, and their momenta and directions are smeared according to the corresponding tracking resolutions. Figure 6 shows the extracted momentum, polar angle, and azimuthal angle resolutions for scattered electrons and recoil protons as functions of Q^2. In general, the resolutions improve with increasing Q^2. The electron momentum is reconstructed more precisely than the proton momentum, whereas the proton typically exhibits better angular resolution than the electron.

In addition to detector effects, the simulation includes smearing associated with the incoming beams, including the beam energy spread, angular divergence, transverse beam position distribution, and the additional energy variation induced by the crab-cavity system. The reconstructed electron and proton four-momenta are then used to characterize the elastic-event topology and calculate the relevant kinematic variables. In particular, the DA method described in Section 4 uses the measured polar angles of the outgoing electron and proton to reconstruct y, Q^2, and x. Because this method depends primarily on angular measurements, its performance benefits directly from the broad angular coverage and tracking resolution of the EicC central detector.

The kinematic distributions shown in Figure 2 indicate that, for the 3.5 GeV electron and 20 GeV proton beam configuration, both scattered electrons and recoil protons lie within an experimentally accessible pseudo-rapidity region over the Q^2 range considered. As Q^2 increases, the electron moves from the backward region toward η approximately

0, while the recoil proton remains within the ion-endcap region of the central detector. The corresponding energy distributions in Figure 3 show that both final-state particles have sufficiently high energies for reliable charged-particle tracking, while the scattered electron can additionally be identified using the electromagnetic calorimeter. These kinematic features indicate that the EicC central detector provides the acceptance and tracking capabilities required to reconstruct high-Q^2 elastic ep candidates and evaluate their separation from inelastic backgrounds.

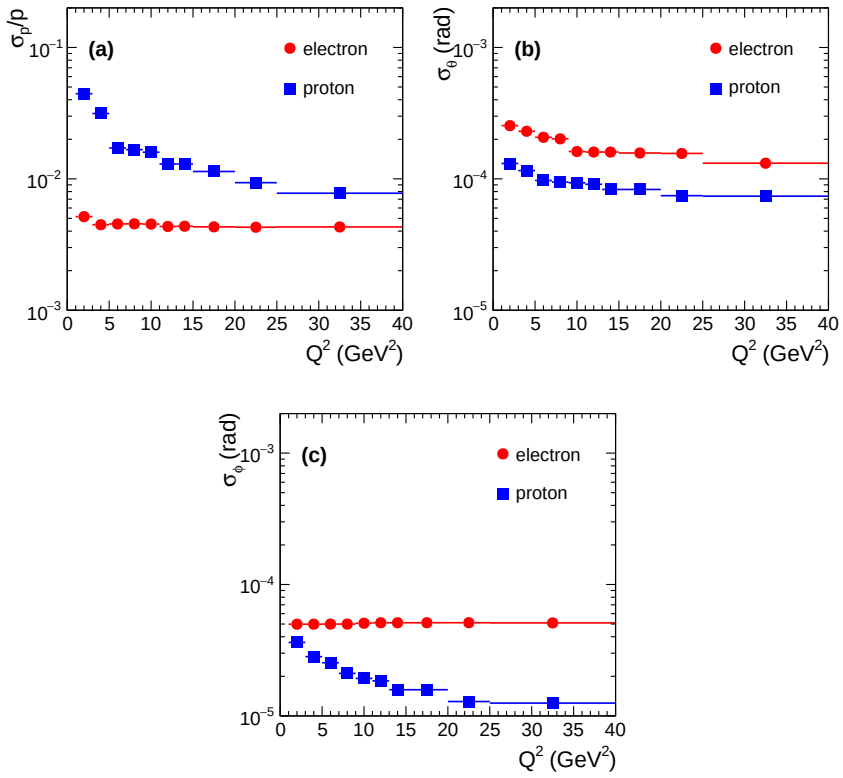


Figure 6. Momentum (**a**), polar angle (**b**), and azimuthal angle (**c**) resolutions for scattered electrons and recoil protons as functions of the true Q^2.

4. Reconstruction

To identify elastic ep events for a given beam energy configuration, two aspects of the event kinematics must be reconstructed: the squared four-momentum transfer, Q^2, and a variable that quantifies the consistency of the event with the elastic final state. The latter is commonly characterized through the invariant mass of the hadronic final state, W, for which elastic scattering corresponds to $W = M_p$, or equivalently through the Bjorken scaling variable x, for which the elastic peak occurs at $x = 1$. In the present study, we use the reconstructed x distribution to identify the elastic peak, while the reconstructed Q^2 determines the kinematic bin in which the event yield is evaluated.

Because elastic scattering is a two-body process, its kinematics can, in principle, be reconstructed from either the scattered electron or the recoil proton alone. With perfect knowledge of the final-state kinematics, elastic and inelastic events could be separated using a single arm. In a realistic measurement, however, detector resolution and beam-related effects smear the reconstructed observables and substantially reduce this separation power. As shown in Figure 7, the reconstructed scattered electron energy distributions for elastic and inelastic events overlap strongly within the representative pseudo-rapidity interval $-1.1 < \eta < -0.9$. This overlap demonstrates that single-arm reconstruction is

insufficient for a clean event-by-event separation under the detector and beam conditions assumed in this study.

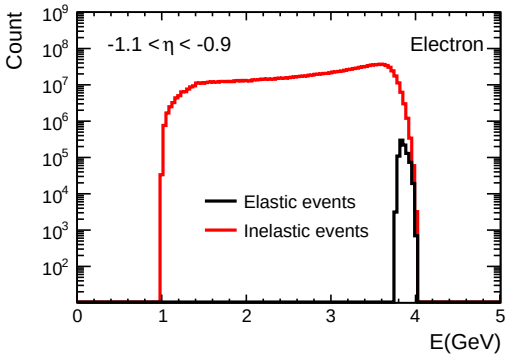


Figure 7. Energy distributions of scattered electrons in the pseudo-rapidity interval $-1.1 < \eta < -0.9$ for elastic (black curve) and inelastic (red curve) ep collisions with 3.5 GeV electrons colliding with 20 GeV protons. The distributions correspond to an integrated luminosity of 100 fb^{-1}.

In the electron method, the kinematic variables are reconstructed from the energy and polar angle of the scattered electron. At small y, however, the relative resolution of the reconstructed x increases approximately as $\delta x_e/x_e \propto 1/y$ [43]. Because the elastic events considered at the EicC occupy the low-y region ($y < 0.15$) for $Q^2 < 40$ GeV^2, realistic uncertainties in the electron energy and angle lead to a broad reconstructed elastic peak in x_e. An alternative is the Jacquet–Blondel (JB) method, in which the event kinematics are reconstructed from the hadronic final state. For an elastic event, this corresponds to using the measured recoil proton momentum. Previous studies for the U.S. EIC found that the JB method produces a visible elastic peak in x, but gives a substantially poorer Q^2 resolution than the electron method [43].

We therefore employ the DA method, which reconstructs the event kinematics using the measured polar angles of both scattered electrons and recoil protons [43]. The DA variables are given by

$$\begin{aligned} y_{\mathrm{DA}} &= \frac{\tan(\theta_p/2)}{\tan(\theta_e/2)+\tan(\theta_p/2)}, \\ Q^2_{\mathrm{DA}} &= 4E_e^2 \frac{\cot(\theta_e/2)}{\tan(\theta_e/2)+\tan(\theta_p/2)}, \\ x_{\mathrm{DA}} &= \frac{Q^2_{\mathrm{DA}}}{s y_{\mathrm{DA}}}, \end{aligned} \tag{4}$$

where $s = 4E_eE_p$ is the square of the center-of-mass energy. These relations are obtained by imposing the kinematic constraints of a two-body elastic final state. Consequently, for true elastic events, Q^2_{DA} provides a reconstruction of the physical momentum transfer and x_{DA} peaks near unity. When the same expressions are applied to inelastic events, the reconstructed quantities do not necessarily correspond to their true DIS values. Instead, x_{DA} measures how closely the observed electron–proton pair satisfies the elastic hypothesis and can therefore be used as an elastic event discriminator.

The reconstruction performance for elastic events is shown in Figure 8. The DA method provides a narrow correlation between the reconstructed and true values of Q^2 over the kinematic range considered. The reconstructed x_{DA} distribution also remains concentrated near the elastic value of unity, allowing the elastic peak to be defined more clearly than with the electron-only or JB methods. This improvement arises because the DA method depends primarily on the complementary angular measurements of the two final-state particles and is less directly sensitive to their momentum resolutions. The achievable resolution never-

theless remains affected by the detector angular resolutions, as well as various beam effects, such as angular divergence of the beams and transverse interaction-point distributions.

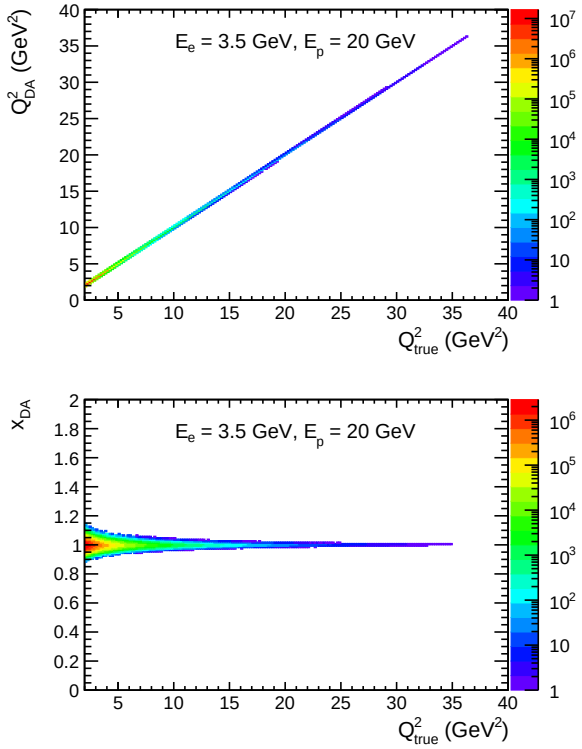


Figure 8. Reconstructed Q^2 (**top**) and x (**bottom**) for elastic ep events using the DA method, as functions of the true Q^2.

In addition to improving the reconstruction of Q^2 and the elastic peak, measuring both final-state particles provides several independent consistency checks. The DA variables can be combined with the electron–proton angular correlation, azimuthal back-to-back topology, transverse-momentum balance, and total-energy and longitudinal-momentum constraints. These observables are used in the following section to suppress inelastic backgrounds and select a clean sample of elastic-event candidates.

5. Background

A precise measurement of the elastic ep cross section requires efficient suppression of inelastic backgrounds while retaining a high elastic event efficiency. In this section, we investigate the separation of elastic events from the dominant inelastic contributions considered in this study, namely deep-inelastic scattering (DIS), resonance production, and other low-W inelastic processes under the assumed EicC detector conditions.

The inelastic background is studied using event samples generated independently with PYTHIA [49] and GiBUU [50]. For both generators, the minimum allowed hadronic invariant mass W is set as low as permitted to include events from the resonance region as well as the deep-inelastic regime. The two samples are therefore used as complementary descriptions of the inelastic background over a broad W range. All generated events are processed through the same fast detector simulation described in Section 3, including detector-resolution and beam-related smearing effects. The study is performed for the nominal beam configuration of 3.5 GeV electrons colliding with 20 GeV protons. Events are considered when an electron candidate and a positively charged hadron candidate are reconstructed within the central-detector acceptance, $-3.5 < \eta < 3.5$.

Elastic scattering is characterized by a two-body final state whose measured kinematics are strongly constrained by energy and momentum conservation. Building on the approach developed in Ref. [43], we construct a sequence of topology- and kinematics-based selection criteria to retain elastic events while progressively suppressing inelastic backgrounds. Figure 9 compares the reconstructed distributions for elastic events with those obtained from the PYTHIA inelastic sample. The inelastic distributions are scaled down in the figure for visual clarity. Based on these observables, the following selection criteria are applied sequentially:

- Step 1: Final-state multiplicity and acceptance. Events are required to contain exactly one reconstructed electron candidate and one reconstructed positively charged hadron candidate, with both tracks lying within the central-detector acceptance, $-3.5 < \eta < 3.5$.
- Step 2: Co-planarity. In elastic scattering, the outgoing electron and proton are approximately back-to-back in azimuthal angles. Events are therefore required to satisfy $\left||\phi_p - \phi_e| - \pi\right| < 0.07$ rad, as illustrated in Figure 9a.
- Step 3: Transverse-momentum conservation. The transverse momenta of scattered electrons and recoil protons must be approximately the same in magnitude: $|p_{T,p} - p_{T,e}| < 0.2$ GeV/c, as shown in Figure 9b.
- Step 4: Longitudinal-momentum conservation. The sum of the reconstructed longitudinal momenta should be consistent with the net longitudinal momentum of the incoming beams. The distribution is centered near 16.5 GeV/c, as shown in Figure 9c, and events are required to satisfy 14 GeV/c $< p_{z,\mathrm{tot}} <$ 19 GeV/c.
- Step 5: Total-energy conservation. For a fully reconstructed elastic event, the sum of the final-state electron and proton energies should be consistent with the total incoming beam energy. The reconstructed distribution is centered near 23.5 GeV, as shown in Figure 9d, and the selection requirement is 21 GeV $< E_{\mathrm{tot}} <$ 26 GeV.
- Step 6: Double-angle elastic consistency. The variable reconstructed with the DA method is required to lie near the elastic value: $0.94 < x_{\mathrm{DA}} < 1.06$. The corresponding distribution is shown in Figure 9e. For inelastic events, x_{DA} should be interpreted as a measure of consistency with the elastic two-body hypothesis rather than as an unbiased reconstruction of the true Bjorken x.
- Step 7: Electron energy–pseudo-rapidity correlation. For elastic scattering, the scattered-electron energy is related to its pseudorapidity by

$$E'_{e,\mathrm{elas}}(\eta_e) = \frac{2E_e E_p}{E_e + E_p + (E_e - E_p)\tanh\eta_e}, \tag{5}$$

  where E_e and E_p denote the incoming electron and proton beam energies, respectively. As shown in Figure 9f, elastic events populate a narrow band in the E'_e–η_e plane. Events are accepted when $\left|E'_e - E'_{e,\mathrm{elas}}(\eta_e)\right| < 0.15$ GeV.

A further issue is the limited proton-identification capability at high momentum. As discussed in Section 3, the baseline EicC PID system in the ion-endcap region is expected to provide hadron separation only up to momenta of approximately 15 GeV/c, whereas recoil protons from the elastic events studied here frequently exceed this value. Inelastic events can also contain high-momentum π^+ and K^+ tracks that may be misidentified as protons in the absence of PID information. Figure 10 shows the momentum distributions of positively charged pions and kaons in the PYTHIA inelastic sample. A non-negligible population of pions and kaons extends above 15 GeV/c, demonstrating that high-momentum hadron misidentification must be considered. We therefore evaluate the selection performance under two limiting scenarios: perfect proton identification and no PID separation among π^+, K^+, and proton candidates.

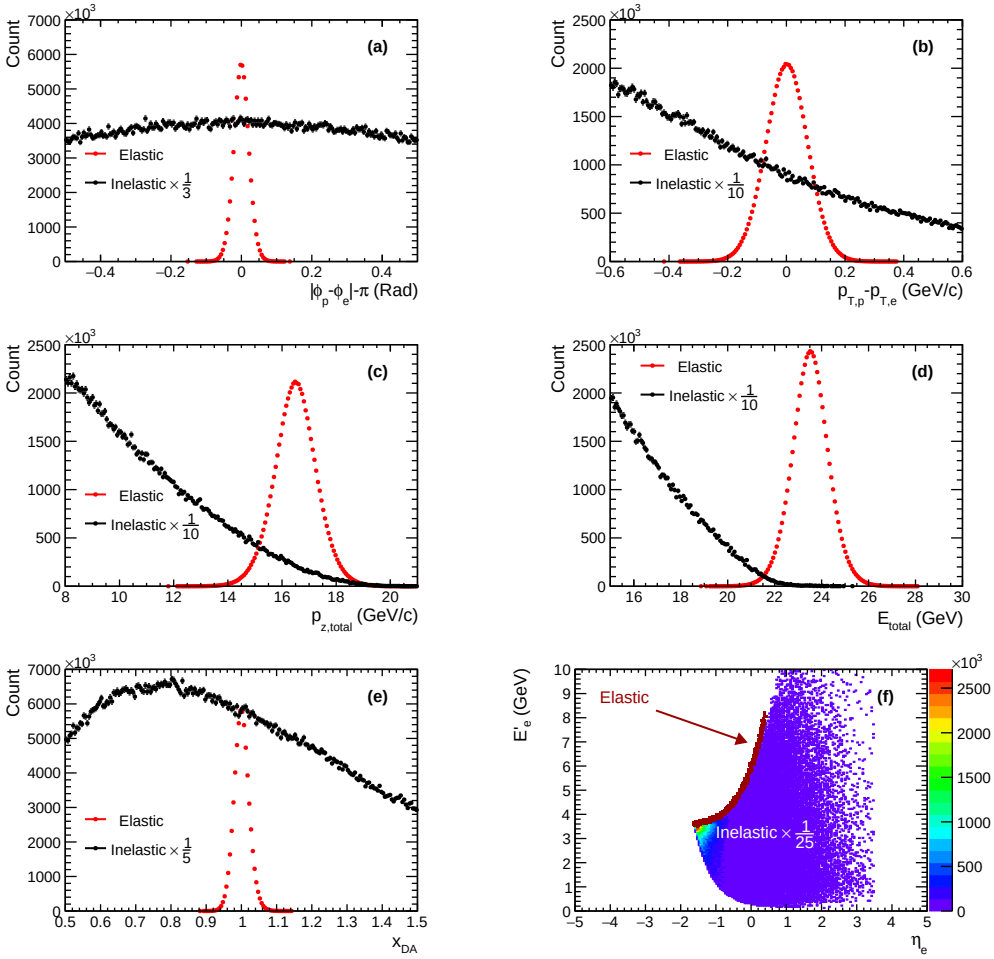


Figure 9. Reconstructed event-topology observables for elastic ep scattering with $Q^2 > 2$ GeV^2 at the EicC for 3.5 GeV electrons colliding with 20 GeV protons: (**a**) deviation from the back-to-back azimuthal configuration, $\big||\phi_p - \phi_e| - \pi\big|$; (**b**) transverse-momentum difference, $p_{T,p} - p_{T,e}$; (**c**) total reconstructed longitudinal momentum, $p_{z,\mathrm{tot}}$; (**d**) total reconstructed energy, E_{tot}; (**e**) x_{DA} reconstructed using the DA method; and (**f**) correlation between the scattered-electron energy, E'_e, and pseudo-rapidity, η_e. All events are processed using the fast detector simulation and normalized to an integrated luminosity of 100 fb^{-1}. The corresponding distributions for inelastic ep events generated with PYTHIA are overlaid for comparison. These background events correspond to the sample before any selection criteria are applied and are scaled down solely for visual clarity. Both final-state candidates are required to lie within the assumed central-detector acceptance, $-3.5 < \eta < 3.5$.

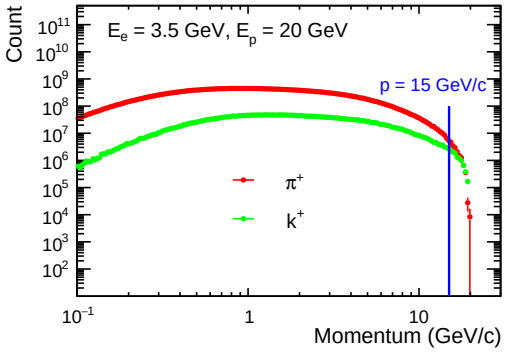


Figure 10. Momentum distributions of positively charged pions (red) and kaons (green) in inelastic ep events generated with PYTHIA. The blue vertical line indicates the momentum above which the baseline PID performance is expected to degrade.

The effects of the sequential selection criteria are summarized in Tables 1 and 2. For the PYTHIA sample, the azimuthal angle and transverse momentum requirements provide substantial initial suppression, while the total energy, x_{DA}, and electron energy–pseudo-rapidity requirements reduce the surviving sample further. No PYTHIA event survives the complete selection sequence in either PID scenario. Similarly, no GiBUU event survives after the electron energy–pseudo-rapidity requirement, even when no PID separation among positively charged hadrons is assumed. After applying the full set of cuts, less than 2% of the signal is accidentally removed, while ∼98.2% of the elastic events are still retained.

Table 1. Sequential suppression of PYTHIA inelastic events with $Q^2 > 2\ \mathrm{GeV}^2$. The second column assumes perfect proton identification, whereas the third assumes no PID separation among positively charged pions, kaons, and protons. Raw simulated event counts are listed first, followed in parentheses by the corresponding yields scaled to an integrated luminosity of 100 fb^{-1}.

Veto Steps	Remaining Event Counts Assuming Perfect Proton Identification (Scaled to 100 fb^{-1})	Remaining Event Counts Assuming No PID for π^+, K^+ or Protons (Scaled to 100 fb^{-1})
All events	1.09×10^7 (1.04×10^{10})	1.09×10^7 (1.04×10^{10})
Step 1	5.51×10^6 (5.00×10^9)	9.93×10^6 (9.12×10^9)
Step 2	2.69×10^5 (2.47×10^8)	5.59×10^5 (4.59×10^8)
Step 3	1.50×10^4 (3.27×10^7)	2.94×10^4 (5.39×10^7)
Step 4	1747 (1.81×10^6)	1889 (1.87×10^6)
Step 5	132 (3.90×10^5)	129 (3.38×10^5)
Step 6	17 (4.70×10^4)	13 (3.27×10^4)
Step 7	0 (0)	0 (0)

Table 2. Sequential suppression of GiBUU resonance and low-W inelastic events with $Q^2 > 2\ \mathrm{GeV}^2$. The second column assumes perfect proton identification, whereas the third assumes no PID separation among positively charged pions, kaons, and protons. Raw simulated event counts are listed first, followed in parentheses by the corresponding yields scaled to an integrated luminosity of 100 fb^{-1}.

Veto Steps	Remaining Event Counts Assuming Perfect Proton Identification (Scaled to 100 fb^{-1})	Remaining Event Counts Assuming No PID for π^+, K^+ or Protons (Scaled to 100 fb^{-1})
All events	4.50×10^7 (1.11×10^{10})	4.50×10^7 (1.11×10^{10})
Step 1	1.57×10^7 (3.75×10^9)	3.74×10^7 (9.08×10^9)
Step 2	3.48×10^5 (8.30×10^7)	8.31×10^5 (2.02×10^8)
Step 3	9465 (4.20×10^6)	1.34×10^4 (5.94×10^6)
Step 4	1579 (6.47×10^5)	1755 (7.25×10^5)
Step 5	394 (1.85×10^5)	417 (1.96×10^5)
Step 6	30 (1.65×10^4)	32 (1.76×10^4)
Step 7	0 (0)	0 (0)

These results demonstrate strong rejection of the simulated DIS, resonance, and low-W background samples under the assumptions of the present fast simulation. However, the absence of surviving events in a finite Monte Carlo sample should not be interpreted as proof of exactly zero physical background. Instead, it establishes an upper limit determined by the generated sample size and its normalization. A quantitative cross section

extraction would therefore require sufficiently large background samples, an estimate of the corresponding statistical upper limits, and studies of additional possible backgrounds and systematic uncertainties. Within the statistical sensitivity of the samples studied here, the combined kinematic selections indicate that a highly pure elastic event sample can be obtained even without direct proton identification at high momentum.

We also studied radiative effects with the ESEPP generator [51], including first-order bremsstrahlung from initial- and final-state leptons and protons, together with virtual-photon corrections. With the same luminosity normalization, detector resolution, beam effects, and selection cuts, the estimated size of the radiative effect is about 20% at low Q^2 and grows to about 40% at $Q^2 = 40$ GeV. Radiative effects are thus important, but a large elastic signal still survives the selection cuts.

6. Summary

We have presented a study of unpolarized elastic ep scattering at the EicC for a 3.5 GeV electron beam colliding with a 20 GeV proton beam. Assuming an integrated luminosity of 100 fb^{-1}, sizable elastic event yields are expected over a broad kinematic range, extending to approximately $Q^2 = 40$ GeV^2 with suitable binning. Such measurements would provide high-Q^2 elastic cross section data in a kinematic region complementary to those accessible at Jefferson Lab and the U.S. EIC.

Over the Q^2 range considered, both scattered electrons and recoil protons can be reconstructed within the assumed central-detector acceptance. The event kinematics are reconstructed using the DA method, which exploits the measured polar angles of both final-state particles and provides good resolutions in Q^2 and in the reconstructed elastic peak near $x = 1$. Although either final-state particle is sufficient in principle to determine the kinematics of an elastic event, detecting both particles improves the reconstruction and overconstrains the two-body final state, thereby providing strong discrimination against inelastic backgrounds. The simulated inelastic backgrounds are suppressed using a sequence of topology- and kinematics-based selection criteria. No background event survives the complete selection sequence in the available PYTHIA or GiBUU samples for $Q^2 > 2$ GeV^2, even when no direct PID separation among high-momentum positively charged hadrons is assumed. This result demonstrates strong background rejection within the statistical sensitivity of the simulated samples, although larger Monte Carlo samples and data-driven studies will be required to quantify the residual background and its associated uncertainty. The accessible elastic events are concentrated at values of ε close to unity. The beam-energy configurations considered here therefore do not provide a sufficiently broad ε lever arm for an independent Rosenbluth separation of G_E and G_M. Instead, an EicC measurement could provide precise elastic cross section data in the high-ε region, offering complementary constraints on the proton electromagnetic form factors. Such data could be incorporated into global analyses combining existing cross section and polarization measurements [34,39].

Overall, the projected event yields, central-detector acceptance, double-angle reconstruction performance, and suppression of the simulated inelastic backgrounds indicate that a clean sample of high-Q^2 elastic ep events could be identified at the EicC. These results provide an initial basis for further studies of detector performance, radiative effects, systematic uncertainties, and the eventual extraction of elastic cross sections and proton electromagnetic form factors.

Author Contributions: Conceptualization, W.X.; methodology, W.C. and W.X.; software, Y.L. and W.X.; validation, W.C., Y.L. and W.X.; formal analysis, W.C.; investigation, W.C. and W.X.; data curation, Y.L. and W.X.; supervision, W.X. All authors contribute equally to the draft preparation, review, and editing. All authors have read and agreed to the published version of the manuscript.

Funding: The work of Weizhi Xiong and Yutie Liang is supported by the National Key Research and Development Project of China under Contract No. 2023YFA1606800. Weizhi Xiong is also supported by the Shandong Province Natural Science Foundation under Grant No. 2023HWYQ-010. The work of Wan Chang is supported by the National Natural Science Foundation of China with Grant No. 12305144.

Data Availability Statement: The original contributions presented in this study are included in the article. Further inquiries can be directed to the corresponding author.

Acknowledgments: The authors would like to thank Yi Chen for his careful reading of the manuscript and for his valuable comments and suggestions.

Conflicts of Interest: The authors declare no conflicts of interest.

References

1. Ernst, F.J.; Sachs, R.G.; Wali, K.C. Electromagnetic form factors of the nucleon. *Phys. Rev.* **1960**, *119*, 1105–1114. [CrossRef]
2. Sachs, R.G. High-Energy Behavior of Nucleon Electromagnetic Form Factors. *Phys. Rev.* **1962**, *126*, 2256–2260. [CrossRef]
3. Perdrisat, C.F.; Punjabi, V.; Vanderhaeghen, M. Nucleon Electromagnetic Form Factors. *Prog. Part. Nucl. Phys.* **2007**, *59*, 694–764. [CrossRef]
4. Arrington, J.; Roberts, C.D.; Zanotti, J.M. Nucleon electromagnetic form-factors. *J. Phys. G Nucl. Part. Phys.* **2007**, *34*, S23. [CrossRef]
5. Punjabi, V.; Perdrisat, C.F.; Jones, M.K.; Brash, E.J.; Carlson, C.E. The Structure of the Nucleon: Elastic Electromagnetic Form Factors. *Eur. Phys. J. A* **2015**, *51*, 79. [CrossRef]
6. Gao, H.; Vanderhaeghen, M. The proton charge radius. *Rev. Mod. Phys.* **2022**, *94*, 015002. [CrossRef]
7. Yennie, D.R.; Lévy, M.M.; Ravenhall, D.G. Electromagnetic Structure of Nucleons. *Rev. Mod. Phys.* **1957**, *29*, 144. [CrossRef]
8. Burkardt, M. Impact parameter space interpretation for generalized parton distributions. *Int. J. Mod. Phys. A* **2003**, *18*, 173–208. [CrossRef]
9. Miller, G.A. Charge Density of the Neutron. *Phys. Rev. Lett.* **2007**, *99*, 112001. [CrossRef]
10. Carlson, C.E.; Vanderhaeghen, M. Empirical transverse charge densities in the nucleon and the nucleon-to-Delta transition. *Phys. Rev. Lett.* **2008**, *100*, 032004. [CrossRef]
11. Lorcé, C. Charge Distributions of Moving Nucleons. *Phys. Rev. Lett.* **2020**, *125*, 232002. [CrossRef]
12. Kim, J.Y.; Kim, H.C. Transverse charge distributions of the nucleon and their Abel images. *Phys. Rev. D* **2021**, *104*, 074003. [CrossRef]
13. Li, Y.; Dong, W.B.; Yin, Y.L.; Wang, Q.; Vary, J.P. Minkowski's lost legacy and hadron electromagnetism. *Phys. Lett. B* **2023**, *838*, 137676. [CrossRef]
14. Panteleeva, J.Y.; Epelbaum, E.; Gegelia, J.; Meißner, U.G. Definition of electromagnetic local spatial densities for composite spin-1/2 systems. *Phys. Rev. D* **2022**, *106*, 056019. [CrossRef]
15. Chen, Y.; Lorcé, C. Pion and nucleon relativistic electromagnetic four-current distributions. *Phys. Rev. D* **2022**, *106*, 116024. [CrossRef]
16. Chen, Y.; Lorcé, C. Nucleon relativistic polarization and magnetization distributions. *Phys. Rev. D* **2023**, *107*, 096003. [CrossRef]
17. Freese, A.; Miller, G.A. Light front synchronization and rest frame densities of the proton: Electromagnetic densities. *Phys. Rev. D* **2023**, *107*, 074036. [CrossRef]
18. Chen, L.B.; Chen, W.; Feng, F.; Hu, S.; Jia, Y. Next-to-Leading-Order QCD Corrections to Nucleon Dirac Form Factors. *Phys. Rev. Lett.* **2025**, *135*, 131903. [CrossRef]
19. Huang, Y.K.; Shi, B.X.; Wang, Y.M.; Zhao, X.C. Next-to-Leading-Order QCD Predictions for the Nucleon Form Factors. *Phys. Rev. Lett.* **2025**, *135*, 061901. [CrossRef]
20. Yao, Z.Q.; Binosi, D.; Cu, Z.F.; Roberts, C.D. Nucleon charge and magnetisation distributions: Flavour separation and zeroes. *arXiv* **2024**, arXiv:2403.08088.
21. Cheng, P.; Yao, Z.Q.; Binosi, D.; Lu, Y.; Roberts, C.D. Quark + diquark description of nucleon elastic electromagnetic form factors. *Eur. Phys. J. A* **2025**, *61*, 255. [CrossRef]
22. Binosi, D.; Roberts, C.D.; Yao, Z.Q. Hadron Structure: Perspective and Insights. *PoS* **2025**, *483*, 001. [CrossRef]
23. Sufian, R.S.; de Téramond, G.F.; Brodsky, S.J.; Deur, A.; Dosch, H.G. Analysis of nucleon electromagnetic form factors from light-front holographic QCD: The spacelike region. *Phys. Rev. D* **2017**, *95*, 014011. [CrossRef]
24. Chambers, A.J. et al. [QCDSF/UKQCD/CSSM Collaborations] Electromagnetic form factors at large momenta from lattice QCD. *Phys. Rev. D* **2017**, *96*, 114509. [CrossRef]
25. Batelaan, M. et al. [QCDSF-UKQCD-CSSM Collaboration] Nucleon Form Factors from the Feynman-Hellmann Method in Lattice QCD. *PoS* **2022**, *396*, 426. [CrossRef]
26. Syritsyn, S.; Engelhardt, M.; Krieg, S.; Negele, J.; Pochinsky, A. Nucleon electromagnetic form factors at large momentum from Lattice QCD. *PoS* **2025**, *466*, 340. [CrossRef]

27. Jones, M.K. et al. [Jefferson Lab Hall A Collaboration] G_{Ep}/G_{Mp} ratio by polarization transfer in $\vec{e}p \to e\vec{p}$. *Phys. Rev. Lett.* **2000**, *84*, 1398–1402. [CrossRef]
28. Gayou, O. et al. [Jefferson Lab Hall A Collaboration] Measurement of G_{Ep}/G_{Mp} in $\vec{e}p \to e\vec{p}$ to $Q^2 = 5.6$ GeV^2. *Phys. Rev. Lett.* **2002**, *88*, 092301. [CrossRef]
29. Qattan, I.A.; Arrington, J.; Segel, R.E.; Zheng, X.; Aniol, K.; Baker, O.K.; Beams, R.; Brash, E.J.; Calarco, J.; Camsonne, A.; et al. Precision Rosenbluth measurement of the proton elastic form-factors. *Phys. Rev. Lett.* **2005**, *94*, 142301. [CrossRef]
30. Crawford, C.B.; Sindile, A.; Akdogan, T.; Alarcon, R.; Bertozzi, W.; Booth, E.; Botto, T.; Calarco, J.; Clasie, B.; DeGrush, A.; et al. Measurement of the proton electric to magnetic form factor ratio from $^1\vec{H}(\vec{e}, e'p)$. *Phys. Rev. Lett.* **2007**, *98*, 052301. [CrossRef]
31. Puckett, A.J.R.; Brash, E.J.; Jones, M.K.; Luo, W.; Meziane, M.; Pentchev, L.; Perdrisat, C.F.; Punjabi, V.; Wesselmann, F.R.; Ahmidouch, A.; et al. Recoil Polarization Measurements of the Proton Electromagnetic Form Factor Ratio to $Q^2 = 8.5$ GeV^2. *Phys. Rev. Lett.* **2010**, *104*, 242301. [CrossRef]
32. Liyanage, A. et al. [SANE Collaboration] Proton form factor ratio $\mu_p G_E^p/G_M^p$ from double spin asymmetry. *Phys. Rev. C* **2020**, *101*, 035206. [CrossRef]
33. Qattan, I.A.; Arrington, J.; Aniol, K.; Baker, O.K.; Beams, R.; Brash, E.J.; Camsonne, A.; Chen, J.-P.; Christy, M.E.; Dutta, D.; et al. High precision measurements of the proton elastic electromagnetic form factors and their ratio at $Q^2 = 0.50$, 2.64, 3.20, and 4.10 GeV^2. *Phys. Rev. C* **2025**, *112*, 035205. [CrossRef]
34. Arrington, J.; Melnitchouk, W.; Tjon, J.A. Global analysis of proton elastic form factor data with two-photon exchange corrections. *Phys. Rev. C* **2007**, *76*, 035205. [CrossRef]
35. Arrington, J.; Blunden, P.G.; Melnitchouk, W. Review of two-photon exchange in electron scattering. *Prog. Part. Nucl. Phys.* **2011**, *66*, 782–833. [CrossRef]
36. Tomalak, O.; Vanderhaeghen, M. Two-photon exchange correction in elastic unpolarized electron-proton scattering at small momentum transfer. *Phys. Rev. D* **2016**, *93*, 013023. [CrossRef]
37. Afanasev, A.; Blunden, P.G.; Hasell, D.; Raue, B.A. Two-photon exchange in elastic electron–proton scattering. *Prog. Part. Nucl. Phys.* **2017**, *95*, 245–278. [CrossRef]
38. Tomalak, O.; Pasquini, B.; Vanderhaeghen, M. Two-photon exchange contribution to elastic e^- -proton scattering: Full dispersive treatment of πN states and comparison with data. *Phys. Rev. D* **2017**, *96*, 096001. [CrossRef]
39. Christy, M.E.; Gautam, T.; Ou, L.; Schmookler, B.; Wang, Y.; Adikaram, D.; Ahmed, Z.; Albataineh, H.; Ali, S.F.; Aljawrneh, B.; et al. Form Factors and Two-Photon Exchange in High-Energy Elastic Electron-Proton Scattering. *Phys. Rev. Lett.* **2022**, *128*, 102002. [CrossRef]
40. Punjabi, V.; Perdrisat, C.F. The Proton Form Factor Ratio Measurements at Jefferson Lab. *EPJ Web Conf.* **2014**, *66*, 06019. [CrossRef]
41. Wojtsekhowski, B.; Cates, G.; Cisbani, E.; Jones, M.; Franklin, G.; Liyanage, N.; Pentchev, L.; Puckett, A.J.R.; Wines, R. A forward-angle large-acceptance magnetic spectrometer. *arXiv* **2026**, arXiv:2207.04378.
42. Abdul Khalek, R.; Accardi, A.; Adam, J.; Adamiak, D.; Akers, W.; Albaladejo, M.; Al-Bataineh, A.; Alexeev, M.; Ameli, F.; Antonioli, P.; et al. Science Requirements and Detector Concepts for the Electron-Ion Collider: EIC Yellow Report. *Nucl. Phys. A* **2022**, *1026*, 122447. [CrossRef]
43. Schmookler, B.; Pierre-Louis, A.; Deshpande, A.; Higinbotham, D.; Long, E.; Puckett, A.J.R. High Q^2 electron-proton elastic scattering at the future Electron-Ion Collider. *arXiv* **2022**, arXiv:2207.04378.
44. Anderle, D.P.; Bertone, V.; Cao, X.; Chang, L.; Chang, N.; Chen, G.; Chen, X.; Chen, Z.; Cui, Z.; Dai, L.; et al. Electron-ion collider in China. *Front. Phys.* **2021**, *16*, 64701. [CrossRef]
45. Kelly, J.J. Simple parametrization of nucleon form factors. *Phys. Rev. C* **2004**, *70*, 068202. [CrossRef]
46. Tian, Y.; Maity, S.; Li, J.; Wu, Y.; Sha, S.; Liang, Y.; Guo, A.; Zhao, Y.; Lin, D. Design and Performance Simulation of the Electromagnetic Calorimeter at EicC. *arXiv* **2025**, arXiv:2512.04432.
47. Li, X.; Zhao, Y.; Liang, Y.; Sun, X. Conceptual Design of PID Detectors for the EicC Spectrometer. *arXiv* **2026**, arXiv:2512.04432.
48. Hoppner, C.; Neubert, S.; Ketzer, B.; Paul, S. A Novel Generic Framework for Track Fitting in Complex Detector Systems. *Nucl. Instrum. Meth. A* **2010**, *620*, 518–525. [CrossRef]
49. Bierlich, C.; Chakraborty, S.; Desai, N.; Gellersen, L.; Helenius, I.; Ilten, P.; Lönnblad, L.; Mrenna, S.; Prestel, S.; Preuss, C.T.; et al. A comprehensive guide to the physics and usage of PYTHIA 8.3. *SciPost Phys. Codeb.* **2022**, *2022*, 8. [CrossRef]
50. Buss, O.; Gaitanos, T.; Gallmeister, K.; van Hees, H.; Kaskulov, M.; Lalakulich, O.; Larionov, A.B.; Leitner, T.; Weil, J.; Mosel, U. Transport-theoretical Description of Nuclear Reactions. *Phys. Rept.* **2012**, *512*, 1–124. [CrossRef]
51. Gramolin, A.V.; Fadin, V.S.; Feldman, A.L.; Gerasimov, R.E.; Nikolenko, D.M.; Rachek, I.A.; Toporkov, D.K. A new event generator for the elastic scattering of charged leptons on protons. *J. Phys. G Nucl. Part. Phys.* **2014**, *41*, 115001. [CrossRef]

Disclaimer/Publisher's Note: The statements, opinions and data contained in all publications are solely those of the individual author(s) and contributor(s) and not of MDPI and/or the editor(s). MDPI and/or the editor(s) disclaim responsibility for any injury to people or property resulting from any ideas, methods, instructions or products referred to in the content.